

A time series of filament eruptions observed by three eyes from space: from failed to successful eruptions *

Yuan-Deng Shen^{1,2}, Yu Liu¹ and Rui Liu³

¹ National Astronomical Observatories/Yunnan Observatory, Chinese Academy of Sciences, Kunming 650011, China; ydshen@ynao.ac.cn

² Graduate University of Chinese Academy of Sciences, Beijing 100049, China

³ Space Weather Research Laboratory, New Jersey Institute of Technology, University Heights, Newark, NJ 07102–1982, USA

Received 2010 September 21; accepted 2010 December 21

Abstract We present stereoscopic observations of six sequential eruptions of a filament in the active region NOAA 11045 on 2010 Feb 8, with the advantage of the *STEREO* twin viewpoints in combination with Earth's viewpoint from *SOHO* instruments and ground-based telescopes. The last one of the six eruptions is a coronal mass ejection, but the others are not. The flare in this successful one is more intense than in the others. Moreover, the velocity of filament material in the successful one is also the largest among them. Interestingly, all the filament velocities are found to be proportional to the power of their flares. We calculate magnetic field intensity at low altitude, the decay indexes of the external field above the filament, and the asymmetry properties of the overlying fields before and after the failed eruptions and find little difference between them, indicating the same coronal confinement exists for both the failed and successful eruptions. The results suggest that, besides the confinement of the coronal magnetic field, the energy released in the low corona should be another crucial element affecting a failed or successful filament eruption. That is, a coronal mass ejection can only be launched if the energy released exceeds some critical value, given the same initial coronal conditions.

Key words: Sun: filaments — Sun: corona — Sun: magnetic fields — Sun: flares — Sun: coronal mass ejections (CMEs)

1 INTRODUCTION

Filament activities have been extensively studied in solar physics. It is widely accepted that the magnetic field surrounding the filaments plays a key role in their formation, structure, and stability (Tang 1987; Tandberg-Hanssen 1995; Martin 1998), and these filament eruptions are intimately associated with solar flares and coronal mass ejections (CMEs) (Lin & Forbes 2000; Zhang et al. 2001; Zhang 2002; Hudson et al. 2006; Yang et al. 2008; Shen et al. 2010). The three phenomena are suggested to be different manifestations of a single physical process originating from the coronal magnetic field

* Supported by the National Natural Science Foundation of China.

(Harrison 1995; Priest & Forbes 2002; Lin et al. 2003; Jain et al. 2010), but the relationships among them are not well understood.

Failed filament eruptions have been documented in several studies (e.g. Ji et al. 2003; Alexander et al. 2006; Green et al. 2007; Liu et al. 2009). Theoretical and statistical studies indicate that both the gradient of the overlying magnetic field with respect to height and the field intensity at low altitude are key factors in determining the flux rope's ultimate fate (Dow-Hygelund et al. 2005; Kliem & Török 2006; Fan & Gibson 2007; Liu 2008). According to these studies, a slowly decreasing magnetic field gradient and strong field intensity at low altitude favor failed eruptions by strong confinement of the coronal magnetic field. Recently, Liu et al. (2009) reported a failed filament eruption event in which two erupting filaments were covered by overlying asymmetrical coronal loops formed due to imbalanced magnetic flux in the active region; one of the filaments erupted first and then interacted with the other (Liu et al. 2010b); they merged together and moved out resembling an EUV jet but failed to escape from the Sun. Based on these observational facts, Liu et al. (2010b) calculated and compared the confinement ability of symmetric and asymmetric fields and found that the magnetic confinement of an asymmetric field is stronger than that of a symmetric one. Therefore, they suggest that an asymmetric background field is an important factor leading to failed filament eruptions. The above studies imply that a coronal magnetic field distribution and its related configuration are important for us to understand the process of failed filament eruption. However, for the relation between failed and successful filament eruptions in the same coronal conditions, no observational results have been presented so far.

In this paper, we study a filament and its six eruptions, including both failed and successful cases. They are associated with a series of B- and C- class *GOES* soft X-ray (SXR) flares occurring in NOAA AR 11045 (N22, W00) on 2010 Feb 8. The filament is observed to be struggling to escape the solar surface, and it fails a few times due to the obvious confinement of the overlying magnetic fields, but it finally succeeds when a C6.2 flare happens. This successful eruption led to an Earth-directed gradual CME which caused some mild geomagnetic activity about 3.5 d later. We analyze multi-angle and multi-wavelength data for these events in order to fully understand what the main factors are for a filament eruption to fail or become successful. The paper is arranged as follows: in Section 2, we describe the data used in this paper, Section 3 contains the results of this study, and discussion and conclusions are presented in Section 4.

2 OBSERVATIONS

The observations used in this work are listed as follows:

- (1) Full-disk $H\alpha$ images from the $H\alpha$ telescope of Yunnan Astronomical Observatory (YNAO). We use the $H\alpha$ line-centered images with a cadence of 1 min and a pixel size of $1''$, recorded by a $3k \times 2k$ 16 bit CCD camera. The YNAO's observation started at 01:21 UT and ended at 08:49 UT on 2010 Feb 8.
- (2) Full-disk line-of-sight magnetograms and EUV 195 Å images from the Michelson Doppler Imager (MDI) (Scherrer et al. 1995) and the Extreme Ultraviolet Telescope (EIT) (Delaboudinière et al. 1995) aboard the Solar and Heliospheric Observatory (SOHO). The MDI magnetograms have a pixel size of $2''$ and a 96 min cadence, while the EIT 195 Å images have a pixel size of $2.6''$ and the cadence is 12 min.
- (3) Full-disk EUV 195 and 304 Å images are taken by the Extreme Ultraviolet Imager (EUVI) (Wuelser et al. 2004) of the Sun Earth Connection Coronal and Heliospheric Investigation (SECCHI) (Howard et al. 2008) onboard the Solar Terrestrial Relations Observatory (STEREO) spacecraft (Kaiser et al. 2008). On 2010 Feb 8, STEREO Ahead (STEREO-A) and Behind (STEREO-B) spacecrafts provided continuous images simultaneously from two different view-points with a separation angle of about 135° . The images have a pixel resolution of $1.6''$ and a time cadence of 5 (10) min for 195 (304) Å. All of the coronagraph's bright images, which

were taken by the inner coronagraphs (COR1) (Thompson et al. 2003) of SECCHI aboard the *STEREO*, have a field of view (FOV) ranging from 1.4 to 4 solar radii; the pixel resolution is $15''$ and the cadence is 5 min. In the following, we will respectively refer to the images observed by EUVI (COR1) of SECCHI onboard the *STEREO-A* and *STEREO-B* as EUVI-A (COR1-A) and EUVI-B (COR1-B) for convenience.

- (4) The Reuven Ramaty High Energy Solar Spectroscopic Imager (*RHESSI*) (Lin et al. 2002) images are reconstructed by using the Pixon algorithm (Metcalf et al. 1996) of the *RHESSI* data analysis software in SolarSoftWare (SSW). The Pixon algorithm provides a significantly better photometry measurement, accurate position estimation, and allows for the detection of fainter sources. In the image reconstruction, detectors 3–8 are used and the integration time is 1 min around the *RHESSI* flare peak.
- (5) Transition Region and Coronal Explorer (*TRACE*) white light image (Handy et al. 1999). In the study, only one *TRACE* white light image is available and used.

3 ANALYSIS AND RESULTS

3.1 The Failed Filament Eruptions

On 2010 Feb 8, the active filament was located at the center of NOAA AR 11045 (N22, W00), a rapidly evolving active region with emerging magnetic flux around its core. During 00:00 to 04:00 UT, the filament underwent six eruptions, including five failures and one success, and each was accompanied by a small flare. All the associated flares showed short durations and were B- or C- class, and they took place nearly at the same place (cf. Table 1).

Table 1 Information of the Six *GOES* SXR Flares Accompanying the Filament Eruptions in AR 11045 on 2010 Feb 8

No.	Start (UT)	Peak (UT)	End (UT)	Class	Location (from Earth)
1	00:10	00:16	00:18	C1.4	N22E02
2	01:10	01:14	01:16	B5.8	N21E01
3	01:23	01:29	01:31	B7.0	N21E01
4	02:22	02:37	02:40	B7.4	N22W01
5	02:46	02:52	02:56	B8.3	N22W00
6	03:08	03:17	03:23	C6.2	N23W00

Figure 1 is an overview of the active region in multi-angle and multi-wavelength views before the eruptions. The active region exhibited a quadrupole configuration in the MDI magnetogram while the opposite polarities were interlaced with each other (see Fig. 1(a)). The filament is discernible both in the $H\alpha$ line-center and the EUV 195 Å images (see the white arrow in frame (b) and yellow contours in frames (d)–(f)). The contours of the MDI line-of-sight magnetic field in Figure 1 indicate that the filament is located on the magnetic neutral line but is slightly positioned over the negative polarity region; such magnetic field configuration is thought to be an indicator of some filament instability (Martin 1998). Owing to the lack of $H\alpha$ data before 01:21 UT on Feb 8, the filament in the $H\alpha$ line-centered wavelength at 01:21 UT has already been active and is shown as a thick, dark feature in the $H\alpha$ image. On the other hand, the filament exhibited different shapes as viewed from different aspect angles in the same wavelength images, which was mainly due to the projection effect from different viewpoints (see the yellow contours in frames (d)–(f) in Fig. 1).

The first two eruptions are untraceable in $H\alpha$ due to no $H\alpha$ data being available. Fortunately, YNAO made good observations of the rest of the events. In fact, the preceding five filament eruptions could be identified as failed eruption events when taken in combination with other observations. Here, the third one is selected as an example to illustrate the failed eruption process because it is the best observed one of the six events (cf. Fig. 2). The filament is shown as a dark, thick feature

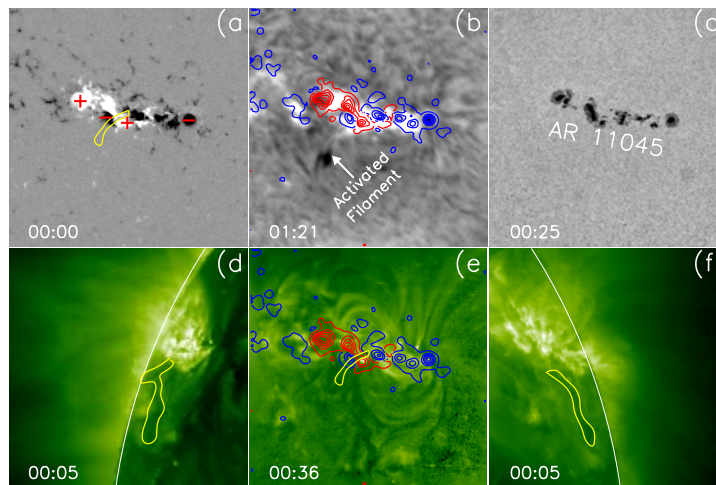


Fig. 1 MDI line-of-sight magnetogram (a), YNAO $H\alpha$ line-center (b), *TRACE* white-light (c), and EUVI-A (d), EIT (e), and EUVI-B (f) 195 Å images before the filament eruptions. The active region is denoted in the *TRACE* white-light image. Contours of MDI magnetic fields are overlaid on the $H\alpha$ and EIT images, in which positive (*negative*) fields are in red (*blue*). The white arrow indicates the active filament, while the filament in the EUV 195 Å images are outlined as yellow contours. In frame (a), the yellow outline is the filament outline in frame (e), and the red + (–) signs label the positive (*negative*) magnetic polarities. The white curves mark the disk limb (the same in the subsequent figures), and the FOV is $380'' \times 380''$ for each frame.

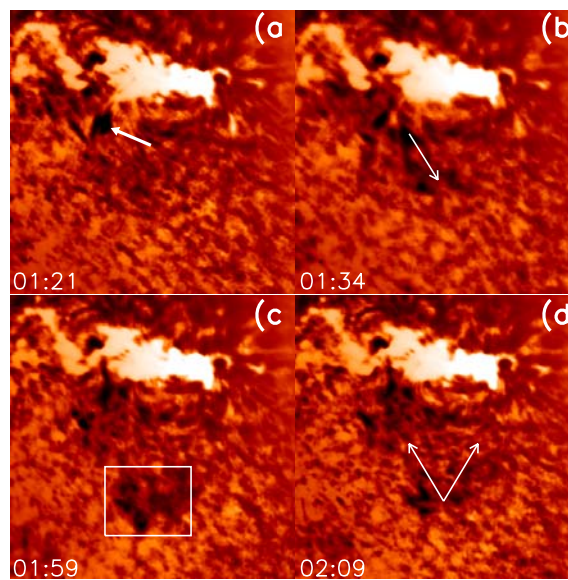


Fig. 2 YNAO $H\alpha$ line-centered images show the filament's main evolution process. The thick white arrow in frame (a) indicates the active filament before eruption, the white thin arrow in frame (b) shows the filament's erupting direction, and the two thin white arrows in (d) show the draining direction of the accumulated plasmoids. The white rectangle is the region where the $H\alpha$ light curve is measured and displayed in Fig. 3. The FOV is $400'' \times 400''$ for each frame.

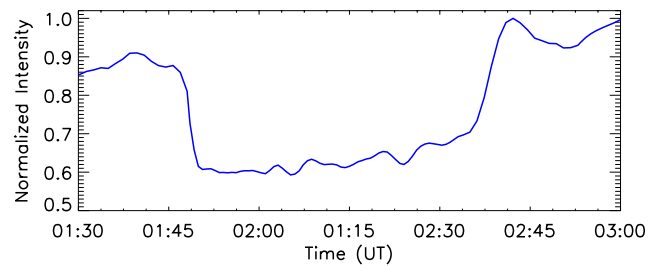


Fig. 3 Normalized light curve in the location where the ejecting filament mass was accumulating as seen from $H\alpha$ observations.

at 01:21 UT just prior to the start of the associated flare (01:23 UT) (see the thick white arrow in Fig. 2(a)), which might indicate the enhanced helical motions in the filament body (Martin 1980; Schmieder et al. 1991). By 01:34 UT, the erupting filament moved out in a configuration similar to a chromospheric surge or a coronal jet along a loop-shaped trajectory (see Fig. 2(b)). Such eruptive filament behavior suggests that the filament was asymmetrically confined by the overlying loops, and its initial moving direction was along the lower part of the loops (Liu et al. 2009). It is interesting to find that the moving plasmoids ceased moving out past about 185 Mm from the primary location. On the contrary, they accumulated there (see Fig. 2(c)) and lasted for a long time before draining back to the solar surface along both legs of the overlying loops (see the two white arrows in Fig. 2(d)). The light curve of the accumulated mass region indicates that the intensity drops suddenly to about 65% of the initial level and then goes through a long gradual recovery process (about 50 min, see Fig. 3). Obviously, the sudden drop of intensity is caused by the intrusion of the dark cold mass of the erupting filament, and the slow drainage motion of the accumulated plasmoids brings about the gradual recovery process.

Figure 4 shows the failed filament eruption process in time sequence of EUVI-A, EIT, and EUVI-B 195 Å raw images. The outer profile of the overlying loops are plotted as fuchsia curves on the EIT 195 Å images. All curves at different times are overlaid on the 02:48 UT frame for comparison and the order numbers are also labeled. The *RHESSI* HXR sources show the associated flare was occurring near the loop's east footpoint. In fact, this region is the area with emerging magnetic flux where magnetic cancellations take place.

The most impressive characteristics in EUV 195 Å are the dynamic behavior of the filament eruption coupled with the overlying loops. The cool, dense filament is exhibited as dark absorption structure in the EUV wavelength due to its relatively low temperature (see the red arrows in Fig. 4). By 01:25 UT, the filament has already experienced the eruption process. It was moving along below the overlying loops instead of escaping (see the red arrow in Fig. 4(b1)); this indicates that the erupting filament was confined by the overlying loops. Similar to the $H\alpha$ line-center observations, the moving filament material stopped and accumulated near the loop top. In the course of the filament eruption, the overlaying loop system experienced an expansion and contraction process, which should be due to the interaction of the erupting filament (compare curves in Fig. 4(b4)). At 02:00 UT, the stretched loops exhibited a cusp structure in the EIT 195 Å images, and the top section was obviously brighter than both its legs (see Fig. 4(b3)). The brightening is thought to be due to the accumulating hot plasmoids. After this moment, the loops begin to slowly contract inward. It is worthwhile to note that the loop expansion (contraction) process observed in EUV 195 Å is in good correspondence to the outward filament (draining back) motion observed in the $H\alpha$ line-center on temporal and spatial scales; this implies that the filament eruption indeed failed at different levels of

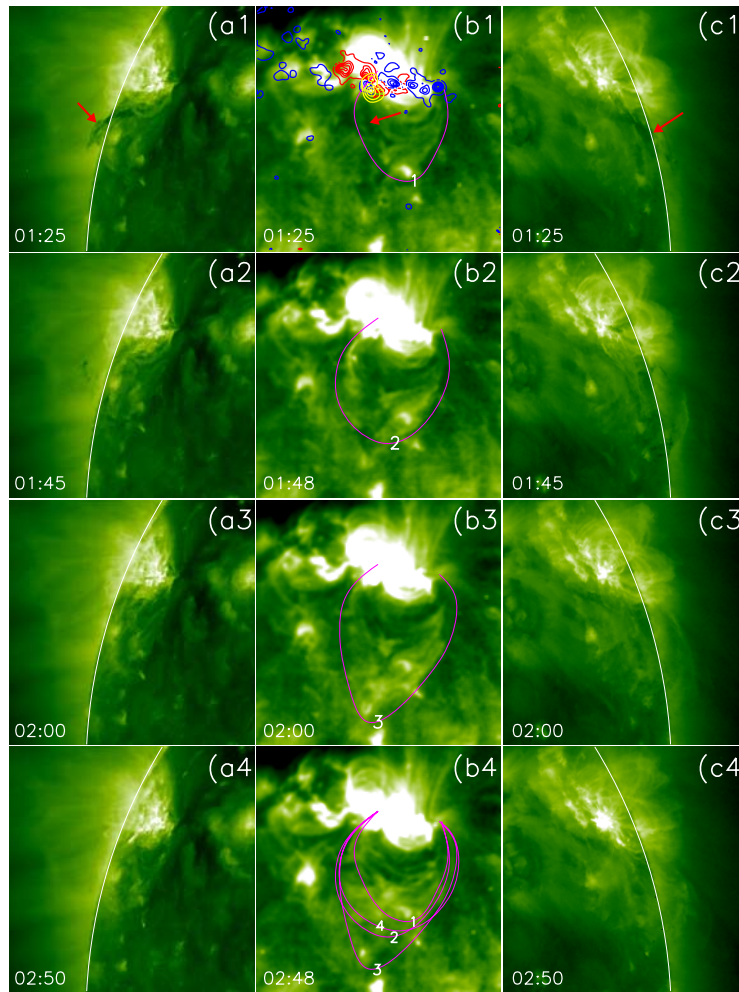


Fig. 4 Time sequences of EUVI-A (a1–a4), EIT (b1–b4), and EUVI-B (c1–c4) 195 Å images. The red arrows indicate the dark filament and the fuchsia curves represent the profile of the overlying loops. The MDI magnetic field at 01:39 UT is overlaid on frame (b1) as red (*positive*) and blue (*negative*) contours, while the yellow contours are the *RHESSI* HXR sources at 01:27 UT, and the contour levels are 35%, 50%, 70%, and 90% of the maximum brightness. The FOV is $450'' \times 450''$ for each frame.

the solar atmosphere. The same evolution process can be identified from both EUVI-A and EUVI-B 195 Å images, but the projection effect needs to be added (see the left and right rows of Fig. 4).

We cannot find any corresponding CME for this event from the databases of COR1-A, COR1-B, and LASCO (Brueckner et al. 1995); these coronagraphs are continuously monitoring CMEs from three different angles. Furthermore, on 2010 Feb 8, the active region was located near the solar central meridian passage in the *SOHO* observation, while it was near the disk limb when observed from the *STEREO* twin viewpoints. Therefore, if a CME originates from this active region, it is expected to be recorded by at least one coronagraph. Based on the above analysis, we conclude that this filament eruption is definitely a failed event.

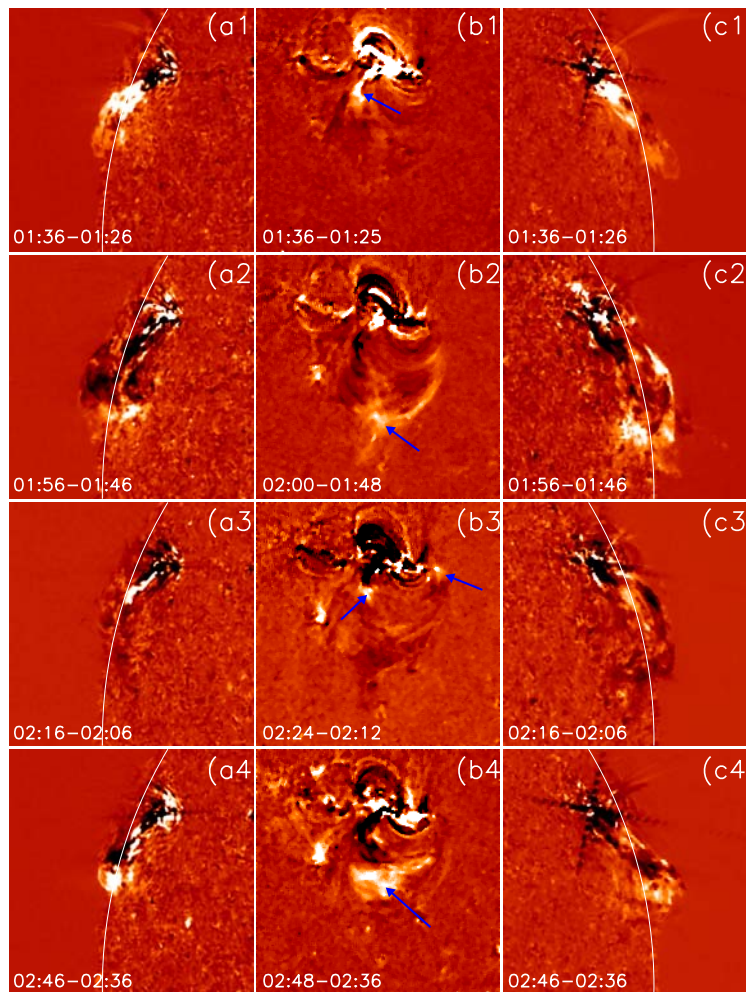


Fig. 5 Time sequences of running difference images of EUVI-A 304 Å (a1–a4), EIT 195 Å (b1–b4), and EUVI-B 304 Å (c1–c4). Blue arrows indicate the moving erupting filament, and the FOV is $500'' \times 500''$ for each frame.

The EUVI-A and EUVI-B 304 Å and EIT 195 Å running difference images are shown in Figure 5, demonstrating the kinematics of the overlying loops confining the filament. We trace the white features, which represent the moving filament material, in time sequences images. It is clear to see that the filament started to erupt from its primary site and kept moving along the overlaying loops. However, it stopped when it reached the loop top. The top and the west parts of the loops were obviously brightened because of the injection of the heated filament mass around 02:00 UT (see the blurred arrows in the top two rows of Fig. 5). The blue arrows, in frame (b3) of Figure 5, point to two white patches where the receding filament material was falling. Meanwhile, the dimming region, formed in the top loop section, indicates mass being evacuated (see Fig. 4(c3)). It is mainly due to the downward motion of the accumulated plasmoids within the confined space of the overlying loops. Later, a brighter patch appeared at 02:48 UT near the loop top (see the blue arrow in Fig. 5(b4)); it was caused by another contiguous filament eruption. Obviously, the brightening patch

was now closer to the original location of the filament compared to Figure 5(b2). This indicates that the whole loop system has contracted after expanding during the previous eruption event (also refer to the fuchsia curves in Fig. 4(b4)), therefore, the erupting filament was confined at a lower height and endured more confinement of the contracted loops because the magnetic fields around the loop top should become more horizontal (Hudson et al. 2008; Wang & Liu 2010).

Based on the above analysis of the eruption events (Nos. 3 and 4 of Table 1), using multi-angle and multi-wavelength observations we believe that the eruptions are really failures and have been well confined by closed coronal fields. It should be pointed out that studies using only single viewpoint data may result in an incorrect conclusion. The occulter of a coronagraph may obscure a low-brightness CME, especially when the eruption occurs from the disk center and heads along

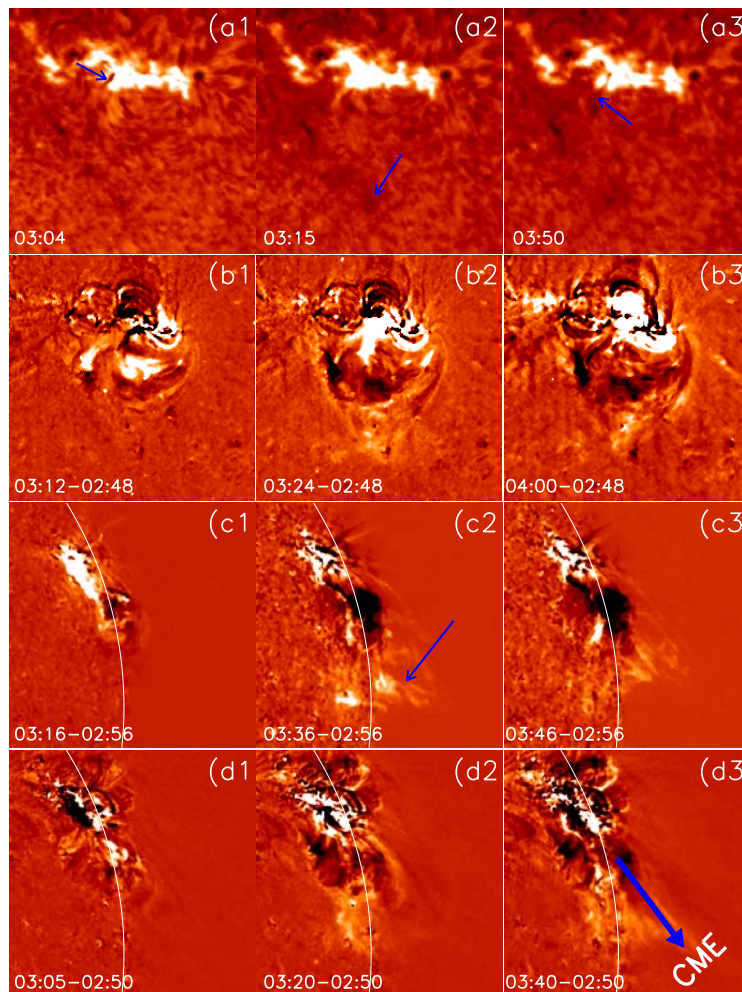


Fig. 6 YNAO $H\alpha$ line-centered images (a1–a3), and the fixed-base difference images of EIT 195 Å (b1–b3), EUVI-B 304 Å (c1–c3) and EUVI-B 195 Å (d1–d3). The short blue arrows indicate the filament at different times in the $H\alpha$ wavelength. The long thin blue arrow indicates the broken site of the filament in EUVI-B 304 Å while the long thick blue arrow shows the filament escaping in EUVI-B 195 Å images. The FOV is $600'' \times 600''$ for all frames.

the line-of-sight direction to the coronagraph. In the following subsection, by using the subsequent successful filament eruption event, we will show how important it is to use stereoscopic data for more reliable CME detection.

3.2 The Successful Filament Eruption

After a series of failed eruptions listed in Table 1 (Nos. 1–5), a subsequent successful filament eruption was observed by *STEREO* EUVI and COR1 telescopes (No. 6, Table 1). The eruption occurred following the end of the fifth failed eruption and was accompanied by a *GOES* SXR C6.2 flare. Unlike the failed eruptions analyzed in the above sections, part of the filament mass successfully escaped from the Sun and a CME was detected by COR1-A and COR1-B. The event process is clearly shown in Figure 6. The top row shows the filament before, during, and after the eruption in $H\alpha$ images. It starts to erupt around 03:04 UT and moves along a loop-like trajectory in a way similar to the preceding failed eruptions (see the short blue arrow in Fig. 6(a2)). The filament, however, changed near its primary location shortly after the eruption (see the short blue arrows in Fig. 6(a3)), which could be regarded as direct evidence for partial filament eruption (Tripathi et al. 2009). In the EUV observation, the evolution process of the filament in EIT 195 Å is also similar to the preceding failed eruptions. However, the upper part of the filament is identified to be ejecting into interplanetary space in the EUVI-B 304 Å difference images, and the broken site is indicated by the long thin blue arrow in Figure 6(c2). The bottom row is the EUVI-B 195 Å difference images, from which the opening process of the overlying loops could be identified and the escaping part is indicated by the long thick blue arrow (Fig. 5(d3)). Although some surface phenomena such as an EIT wave and corona dimming are observed to be associated with this event from the *SOHO/LASCO* database, no CME can be found from it.

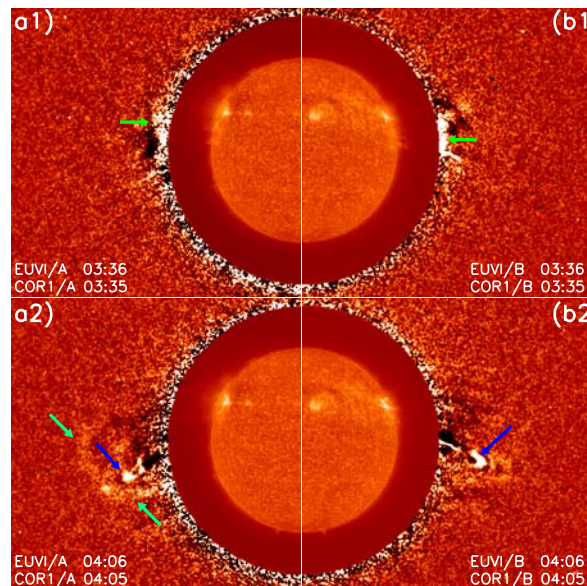


Fig. 7 Composite images of inner EUVI 304 Å and outer COR1 difference images, showing the associated CME of the partial filament eruption. The left row is *STEREO*-A data and the right is *STEREO*-B.

Following the partial eruption, however, an associated CME was obviously observed from the side by COR1-A and COR1-B, although it was not caught by the LASCO telescope. Figure 7 shows the CME evidence in the composite images. A close temporal and spatial relationship between the CME and the erupting filament can be identified from the images. The bright front of the CME first appeared at 03:36 UT in both coronagraphs' FOV (see the two thick green arrows in Fig. 7). The three typical components (viz., a bright front, a dark cavity and a bright compact core) of the CME are clearly observed in COR1-A at 04:05, but are slightly fainter in COR1-B for the CME front. The bright front (compact core) is indicated by the green (blue) arrows in the bottom row of Figure 7. The CME average velocity measured from COR1-A is about 548 km s^{-1} , i.e., a gradual CME.

Because it is always easier to observe a CME initiated at the disk limb than on the disk, it is not surprising that the CME event cannot be detected by the LASCO telescope. The case presented in this section is a good example to show the importance of using stereoscopic observations. If only using the data from the EIT and LASCO instruments, one might mistakenly consider it as a failed filament eruption.

3.3 Relation between Flare Power and Filament Ejection

Figure 8 shows the average filament velocity during the rising phases as a function of the SXR flare energy class. The data are measured from EUVI-A and EUVI-B 195 \AA images respectively. The data distribution of the C1.3 flare, associated with a failed filament eruption studied by Liu et al. (2009), obviously deviates from other points, which is possibly due to the fact that its velocity was measured from $\text{H}\alpha$ wavelengths. The average filament velocity of the C1.3 flare event does not exceed the calculated values for the corresponding class of flares in our study. Generally, a positive correlation is found between the filament velocity and flare power based on the current data. From the result, we can conclude that a filament tends to obtain more kinetic energy which was probably transformed from the magnetic energy released in a bigger flare associated with reconnection than from a smaller one. These results support the statistical study by Morimoto et al. (2010), who found that the thermal energy density of the overlying arcade increases with the filament's mechanical energy density. Moreover, if the efficiency of the filament mass transfer is high enough (represented by high velocity) to destroy the original mechanical equilibrium of the flux rope system in the corona, then a reconstruction process of the coronal magnetic field is expected to occur in order to help the system reach another equilibrium, by releasing free magnetic flux helicity in the form of a CME.

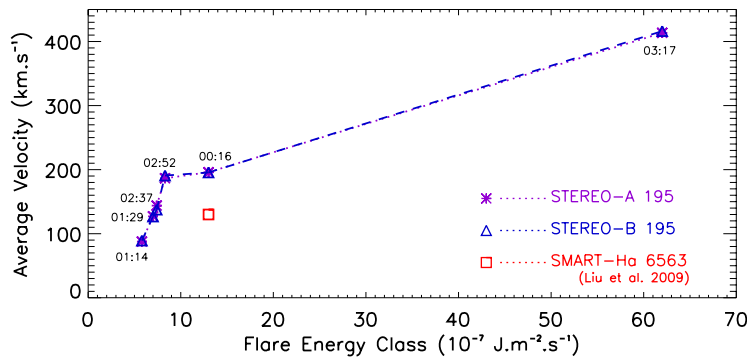


Fig. 8 Average velocity of filament material as a function of *GOES* SXR flare energy class. The asterisks (*triangles*) represent *STEREO-A* (*STEREO-B*) data. The single isolated *red square* (color online) is the data point taken from Liu et al. (2009). The peak time of the flares is also denoted.

3.4 External Fields Over The Erupting Filament

The gradient of the external fields with respect to height is believed to be an important factor for diagnosis of failed or successful filament eruptions (Kliem & Török 2006; Liu 2008; Liu et al. 2010a). It is usually expressed as the so-called decay index, defined as $n = -d\ln(B)/d\ln(h)$. Here B is the poloidal component of the external potential field above the filament and h is the height measured from the photosphere. The potential field model is used to approximate the external magnetic field, and the poloidal component of the external potential field is represented by the horizontal components of the extrapolated potential field. The potential fields at 00:00 UT (before the failed eruptions) and 03:15 UT (after the failed eruptions) are calculated using the NLFFF (a Non-Linear Force-Free-Field extrapolation program) code (Wheatland et al. 2000), in which the potential field calculations are made in Cartesian geometry by a Green's function approach (Chiu & Hilton 1977). The decay indexes, which are derived from a linear fitting to the data before and after the failed eruptions, are 1.90 and 1.84 (see Fig. 9) respectively.

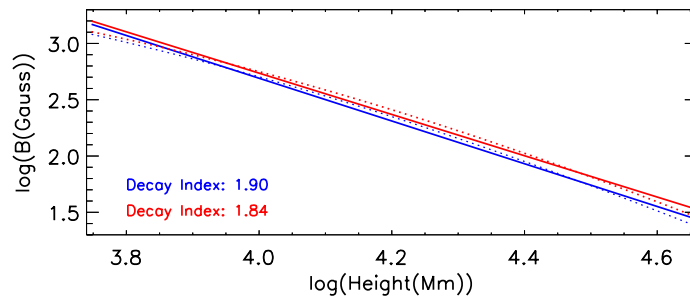


Fig. 9 A fitting of the calculated magnetic field strength and height measured from the photosphere. Here the strength and height are in log units. The *blue (red) dotted line* (color online) is the horizontal component of the potential field before (after) the failed eruptions, while the solid lines are the result of a linear fitting to the data.

In our calculation, the height range is set to 42 to 105 Mm (height range for filament instability; Liu 2008) above the photosphere over the filament eruption location. We also calculate the average decay index in the same height range by setting the step size as the grid spacing (~ 1.41 Mm) in the potential field extrapolation and the results are 1.95 and 1.89. The differences in decay index between the two moments are very small. Regardless of whether a filament eruption is a failure or success, there are two other important factors to consider: the strength of the horizontal field at low altitude and the asymmetric confinements of the overlying fields (Liu 2008; Liu et al. 2009). Hence, we compare the horizontal field at a height of 42 Mm, which is the average height of an eruptive filament, at the two moments based on the potential calculation. The values are 21.5 and 22 Gauss respectively. They are much the same before and after the failed eruptions. Although the filament was asymmetrically confined by the overlying loops (Liu et al. 2009), it is not the primary factor influencing the present study because no obvious morphological change between the two special moments could be identified from the observations. In addition, the ratios of the horizontal field strength at the filament position to the symmetric position at the two moments also show few differences. The above calculation results show that the failed eruptions involving the associated flares do not significantly affect the confinement ability of the external fields. Hence, all the eruptions endured almost the same coronal confinement of the external fields. In addition, the indexes are very close to the upper end of the theoretical critical decay index (1.5–2.0) for successful eruptions (Kliem & Török 2006). This implies that the magnetic system involving the eruptive filament is on the edge

of instability. Since the flares in the failed eruptions are not powerful enough, these results seem to suggest that more energy is needed to cause a successful eruption. The successful eruption associated with a relatively more powerful C6.2 flare in the present study is a good case in point.

4 CONCLUSIONS AND DISCUSSION

The filament eruptions studied in the present paper are associated with a series of B- and C-class flares, in which five are identified as failed eruptions with no CME association and one is a successful eruption with clear evidence of a CME's occurrence. The eruptions are possibly attributed to the emerging magnetic flux around the active region's core where magnetic cancelations are observed between the pre-existing and newly emerging flux. The processes of eruptions are well observed synchronously by ground-based and space-based telescopes, from which multi-angle and multi-wavelength data are available. It should be noted that the successful eruption is a partial filament eruption, and its associated CME is not detected by *SOHO/LASCO* from the Earth's direction but from two other directions in space by the *STEREO/COR1 A* and *B* instruments. During the failed eruption period, the filament is found to be confined by an overlying loop system. The neutral line of the active region, where the filament is located, is very close to the east footpoint of the overlying coronal loops. In the filament eruptions, the mass is observed moving along the overlying loops from the east root in a shape resembling an EUV jet or an $H\alpha$ surge. The filament is observed struggling to escape during the failed eruptions and the tops of the overlying coronal loops are found to be dragged forward and brightened. The filament eruption finally succeeds to escape the Sun when a powerful C6.2 flare takes place, which is accompanied by a CME being launched.

We find that the velocity profile of the erupting filament has a good proportionality relation with the energy class of the associated *GOES* SXR flares. Because the successful filament eruption is associated with a very intensive flare, it seems that the flare's power is an important index in the physical process causing a failed or successful filament eruption. Unfortunately, due to the limited event samples, it is difficult to get the exact critical value for the flare's power, above which a successful filament eruption can be expected for this active region. We believe that a flare with high power is important for us to forecast a successful filament eruption. Based on the potential field extrapolation, we compare the horizontal field at low altitude before and after the failed eruptions and find that the field strengths are much the same. On the other hand, the asymmetric confinement of the overlying fields do not show a conspicuous change at the two moments considered. These results together provide the indication of the same coronal condition for the failed and the successful eruptions.

The failed filament eruptions in our observations are probably due to the following reasons: (1) the stronger field intensity at low altitude, (2) the low magnetic field gradient (decay index) of the overlying loops with height, (3) asymmetrical magnetic confinement of the overlying fields, and (4) sufficiently high kinetic energy for the erupting filament mass. Since the magnetic field intensity, decay index and asymmetry properties are almost the same during the eruptions, the last reason should be a new factor found in this study because the successful eruption event is associated with the most powerful flare, which can supply more kinetic energy to the filament mass by strong outflow from the reconnection involved.

Moreover, some failed filament eruptions have been reported recently in several studies (e.g., Ji et al. 2003; Liu et al. 2009), but all of them are based on single aspect angle observations. When eruptions occurred, the associated CMEs might be obscured by a coronagraph's occulter, so that they may not appear in the coronagraph's FOV for the case of a faint CME launched. To overcome this drawback, multi-angle and multi-wavelength observations are necessary. The eruption in our study speaks volumes for this issue. Hence we should maintain caution on the single angle observations not only for identifying failed filament eruptions but also for analyzing various other forms of solar events.

Acknowledgements We thank the YNAO, *RHESSI*, *TRACE*, *GOES*, *STEREO SECCHI*, and the *SOHO* MDI, EIT and LASCO teams for data support, and the referee for his/her constructive comments. This work is supported by the Chinese foundations MOST (2011CB811400) and the National Natural Science Foundation of China (Grant Nos. 10933003, 11078004 and 11073050).

References

- Alexander, D., Liu, R., & Gilbert, H. R. 2006, *ApJ*, 653, 719
- Brueckner, G. E., Howard, R. A., Koomen, M. J., et al. 1995, *Sol. Phys.*, 162, 357
- Chiu, Y. T., & Hilton, H. H. 1977, *ApJ*, 212, 873
- Delaboudinière, J., Artzner, G. E., Brunaud, J., et al. 1995, *Sol. Phys.*, 162, 291
- Dow-Hygelund, C. C., Holden, B. P., Bouwens, R. J., et al. 2005, *ApJ*, 630, L137
- Fan, Y., & Gibson, S. E. 2007, *ApJ*, 668, 1232
- Green, L. M., Kliem, B., Török, T., van Driel-Gesztelyi, L., & Attrill, G. D. R. 2007, *Sol. Phys.*, 246, 365
- Handy, B. N., Acton, L. W., Kankelborg, C. C., et al. 1999, *Sol. Phys.*, 187, 229
- Harrison, R. A. 1995, *A&A*, 304, 585
- Howard, R. A., Moses, J. D., Vourlidas, A., et al. 2008, *Space Sci. Rev.*, 136, 67
- Hudson, H. S., Bougeret, J., & Burkepile, J. 2006, *Space Sci. Rev.*, 123, 13
- Hudson, H. S., Fisher, G. H., & Welsch, B. T. 2008, in *Astronomical Society of the Pacific Conf. Ser.* 383, eds. R. Howe, R. W. Komm, K. S. Balasubramaniam, & G. J. D. Petrie, 221
- Jain, R., Aggarwal, M., & Kulkarni, P. 2010, *RAA (Research in Astronomy and Astrophysics)*, 10, 473
- Ji, H., Wang, H., Schmahl, E. J., Moon, Y., & Jiang, Y. 2003, *ApJ*, 595, L135
- Kaiser, M. L., Kucera, T. A., Davila, J. M., et al. 2008, *Space Sci. Rev.*, 136, 5
- Kliem, B., & Török, T. 2006, *Phys. Rev. Lett.*, 96, 255002
- Lin, J., & Forbes, T. G. 2000, *J. Geophys. Res.*, 105, 2375
- Lin, J., Soon, W., & Baliunas, S. L. 2003, *Nature*, 47, 53
- Lin, R. P., Dennis, B. R., Hurford, G. J., et al. 2002, *Sol. Phys.*, 210, 3
- Liu, C., Lee, J., Jing, J., et al. 2010a, *ApJ*, 721, L193
- Liu, Y. 2008, *ApJ*, 679, L151
- Liu, Y., Su, J., Shen, Y., & Yang, L. 2010b, in *IAU Symposium*, Vol. 264, eds. A. G. Kosovichev, A. H. Andrei, & J.-P. Roelot, 99
- Liu, Y., Su, J., Xu, Z., et al. 2009, *ApJ*, 696, L70
- Martin, S. F. 1980, *Sol. Phys.*, 68, 217
- Martin, S. F. 1998, *Sol. Phys.*, 182, 107
- Metcalf, T. R., Hudson, H. S., Kosugi, T., Puetter, R. C., & Pina, R. K. 1996, *ApJ*, 466, 585
- Morimoto, T., Kurokawa, H., Shibata, K., & Ishii, T. T. 2010, *PASJ*, 62, 939
- Priest, E. R., & Forbes, T. G. 2002, *A&A Rev.*, 10, 313
- Scherrer, P. H., Bogart, R. S., Bush, R. I., et al. 1995, *Sol. Phys.*, 162, 129
- Schmieder, B., Fontenla, J., & Tandberg-Hanssen, E. 1991, *A&A*, 252, 343
- Shen, Y. D., Li, K. J., Yang, L. H., Yang, J. Y., & Jiang, Y. C. 2010, *Acta Astronomica Sinica*, 51, 151
- Tandberg-Hanssen, E. 1995, *The nature of solar prominences*, *Astrophysics and Space Science Library*, 199
- Tang, F. 1987, *Sol. Phys.*, 107, 233
- Thompson, W. T., Davila, J. M., Fisher, R. R., et al. 2003, in *Society of Photo-Optical Instrumentation Engineers (SPIE) Conf. Ser.* 4853, eds. S. L. Keil & S. V. Avakyan, 1
- Tripathi, D., Gibson, S. E., Qiu, J., et al. 2009, *A&A*, 498, 295
- Wang, H., & Liu, C. 2010, *ApJ*, 716, L195
- Wheatland, M. S., Sturrock, P. A., & Roumeliotis, G. 2000, *ApJ*, 540, 1150
- Wuelser, J., Lemen, J. R., Tarbell, T. D., et al. 2004, in *Society of Photo-Optical Instrumentation Engineers (SPIE) Conf. Ser.* 5171, eds. S. Fineschi & M. A. Gummin, 111
- Yang, L., Jiang, Y., & Ren, D. 2008, *ChJAA (Chin. J. Astron. Astrophys.)*, 8, 329
- Zhang, H. 2002, *MNRAS*, 332, 500
- Zhang, J., Dere, K. P., Howard, R. A., Kundu, M. R., & White, S. M. 2001, *ApJ*, 559, 452